Estimates and Implications of Surface Eddy Diffusivity in the Southern Ocean Derived from Tracer Transport

JOHN MARSHALL

Department of Earth, Atmospheric and Planetary Sciences, Massachusetts Institute of Technology, Cambridge, Massachusetts

EMILY SHUCKBURGH

Department of Applied Mathematics and Theoretical Physics, University of Cambridge, Cambridge, United Kingdom

HELEN JONES AND CHRIS HILL

Department of Earth, Atmospheric and Planetary Sciences, Massachusetts Institute of Technology, Cambridge, Massachusetts

ABSTRACT

Near-surface "effective diffusivities" associated with geostrophic eddies in the Southern Ocean are estimated by numerically monitoring the lengthening of idealized tracer contours as they are strained by surface geostrophic flow observed by satellite altimetry. The resulting surface diffusivities show considerable spatial variability and are large (2000 m^2 s^{-1}) on the equatorward flank of the Antarctic Circumpolar Current and are small (500 m^2 s^{-1}) at the jet axis. Regions of high and low effective diffusivity are shown to be collocated with regions of, respectively, weak and strong isentropic potential vorticity gradients. The maps of diffusivity are used, along with climatological estimates of surface wind stress and air–sea buoyancy flux, to estimate surface meridional residual flows and the relative importance of Eulerian and eddy-induced circulation in the streamwise-averaged dynamics of the Antarctic Circumpolar Current.

1. Introduction

An outstanding problem in large-scale ocean dynamics is the understanding, characterization, and representation of tracer transport by geostrophic eddies, particularly in highly turbulent regions of the ocean, such as the western boundary currents and the Antarctic Circumpolar Current of the Southern Ocean. Eddy transport in the coarse-resolution ocean models used in climate research is parameterized by assuming that eddy tracer flux is related to the mean tracer gradient through an eddy diffusivity K. Arguably, the key uncertainty in these models is lack of knowledge of the magnitude of the Ks and how they vary in space and time. These matters are further complicated because the geographical distribution of eddy transfer is difficult

to characterize by in situ measurements, which by their very nature tend to be local.

Hitherto estimates of K have been inferred from observations in a number of different ways, as follows:

1) Mooring data of time series of velocity $\boldsymbol{v}$ and, for example, temperature T can be used to construct $\overline{\boldsymbol{v}'T'}$ and its relationship to $\nabla \overline{T}$ (see, e.g., Bryden and Heath 1985). However, the time series are rather short (a few years at most) making interpretation difficult, and very few such estimates have been made, raising doubt about how representative they are. Moreover, and more fundamentally, interpretation of such "point" estimates are seriously compromised by the presence of large nondivergent eddy fluxes that play no role in eddy–mean flow interaction (Marshall and Shutts 1981).

2) Floats and drifters do not directly give information about the dispersion of a tracer because they follow particle trajectories rather than tracer concentrations. They can be used to estimate lateral diffusivi-

Corresponding author address: John Marshall, Dept. of Earth, Atmospheric and Planetary Sciences, Room 54-1526, Massachusetts Institute of Technology, Cambridge, MA 02139-4307.
E-mail: jmarsh@mit.edu

ties by measuring components of the diffusivity tensor and dispersion rates, as described in, for example, Davis (1991), Lumpkin et al. (2002), and Zhurbas and Oh (2004). However, such diffusivities are not straightforwardly interpretable in terms of the eddy diffusivities employed in large-scale ocean models.

3) Since the advent of satellite altimetry, our knowledge of eddy statistics at the ocean surface has increased substantially. Holloway (1986) (see also Keffer and Holloway 1988; Stammer 1998; Karsten and Marshall 2002) proposed that eddy diffusivities could be estimated from maps of the rms height field variability using scaling arguments. Kushner and Held (1998) tested the approach in a meteorological context to infer the divergent part of the eddy temperature flux. They emphasized that estimates based on Holloway's method are best interpreted as near-surface diffusivities. The approach is compromised, however, by its reliance on scaling arguments and because the diffusivities so derived are only known up to a "constant of proportionality."

In this paper we attempt to arrive at an alternative estimate of ocean eddy diffusivities using a method pioneered by Nakamura (1996) and applied to diagnose tracer transport in the stratosphere by Haynes and Shuckburgh (2000a,b) and Allen and Nakamura (2001) and to tracer transport in a laboratory setting by Deese et al. (2002). We diagnose transport properties of the eddy field at the ocean's surface by driving an advection–diffusion equation for idealized tracers using 2D nondivergent flow derived from altimetric observations and calculating the "effective diffusivity." The attractiveness of the approach is that, as shown by Nakamura (1996), by adopting an area coordinate, the tracer transport problem can be rigorously phrased as a diffusion problem,

$$\frac{\partial q}{\partial t} = \frac{\partial}{\partial A}\left[\kappa_{\text{eff}}(A)\,\frac{\partial q}{\partial A}\right], \tag{1}$$

where A is the area between a particular q contour and a reference contour, and $\kappa_{\text{eff}}(A)$ depends on integrals of $|\nabla q|^2$ over the area A [the mathematical framework and its connection to earlier work by, e.g., Rhines and Young (1983), is set in the appendix, see section b therein]. The effective diffusivity diagnostic is based on identifying the enhancement of diffusion that arises through the effects of eddies stretching and folding tracer contours. In mixing regions, tracers are vigorously stretched into complex geometrical shapes with tight gradients, and this leads to large values of effective diffusivity. Tracer geometry in regions of barriers is usually smooth, creating localized small values of effective diffusivity that are so small that they keep the flux minimal despite the often large tracer gradients. Because κ_{eff} is diagnosed directly from tracer fields being dispersed by eddies, it is more obviously connected to the surface diffusivities employed in large-scale ocean models than, for example, the diffusivity deduced from the dispersal of floats.

In this study we use Nakamura's (1996) approach to yield *surface* eddy diffusivities associated with horizontal geostrophic eddies measured by altimetry. Surface diffusivities are of special interest and importance because first (and as reviewed by Treguier et al. 1997), quasigeostrophic theory tells us that eddy–mean flow interaction involves interior potential vorticity fluxes and horizontal buoyancy fluxes at the boundary. The two are related to one another, but our diagnostic approach directly yields the surface diffusivities. Second, horizontal boundary eddy fluxes appear as a forcing term on the rhs of the residual-mean buoyancy equation (see Plumb and Ferrari 2005) and can be used, as in Karsten and Marshall (2002), to infer the eddy-induced horizontal circulation at the surface of the ocean associated with eddies.

Our paper is set out as follows. In section 2 we describe how we use altimetric data to drive an advection–diffusion problem for idealized tracers over the Southern Ocean. In section 3 we present our estimates of eddy diffusivities and discuss the robustness of our results. We find that the effective diffusivity exhibits interesting spatial variation, having elevated values (1500–2000 m^2 s^{-1}) on the equatorward flank of the Antarctic Circumpolar Current (ACC), which diminish as the core of the current is approached, to increase again on its poleward flank. We interpret this distribution in terms of the geographical distribution of strain rate and the large-scale potential vorticity (PV) distribution, with the core of the ACC being characterized by large PV gradients that inhibit lateral dispersion. In section 4 we make use of the effective diffusivity to quantify the role of eddies in the streamwise-averaged residual-mean dynamics of the ACC, comparing wind- and eddy-induced cross-stream transport. We argue that mixing by eddies on the equatorial flank of the ACC induces a cross streamflow directed poleward in opposition to the equatorward flow driven directly by the wind. The convergence of these opposed currents induces subduction from the surface into the interior, which we identify as Antarctic Intermediate Water. We conclude in section 5.

2. Diagnostic approach

a. Theoretical background

We are concerned with the problem of a passive tracer q, advected by a two-dimensional nondivergent velocity field $\boldsymbol{v}$, described by the evolution equation

$$\frac{\partial q}{\partial t} + \boldsymbol{v} \cdot \boldsymbol{\nabla}q = k\nabla^2 q, \qquad (2)$$

where k is a constant diffusivity. The advection–diffusion problem has been the subject of numerous investigations dating back to at least Batchelor (1959), see, for example, Rhines and Young (1983) and recent reviews see Majda and Kramer (1999) and Pierrehumbert (2000). In the limit of a large Peclet number $Pe = (VL/k)$, where V and L are the characteristic scales of velocity and eddy length, respectively, diffusion is so small as to make the effect of diffusion appreciable only on very small scales. In the presence of the stirring action of the velocity field, q contours are stretched into complex geometrical shapes driving a general increase in the gradients of q. In the absence of diffusion, the area of fluid demarcated by two tracer contours cannot change, irrespective of how convoluted those contours may become. However, in the presence of k, enhanced gradients of q lead to enhanced mixing and the area contained between q contours changes. By carrying out a census of $|\nabla q|^2$ over the area contained within q contours, an effective eddy diffusivity can be computed as follows.

Nakamura (1996) (see also Winters and D'Asaro 1996) shows that in area coordinates Eq. (2) reduces to Eq. (1) with the diffusivity defined by[1]

$$\kappa_{\text{eff}} = kL_{\text{eq}}^2, \qquad (3)$$

where L_{eq} is the "equivalent length" of a q contour [see appendix, Eq. (A5)]. Note that κ_{eff} has units of meters to the fourth power per second because [see Eq. (1)] it represents diffusion of q in area coordinates. To obtain diffusivity in physical space with units of meters squared per second we define a quantity

$$K_{\text{eff}} = k\frac{L_{\text{eq}}^2}{L_{\text{min}}^2}, \qquad (4)$$

where L_{min} is the minimum (unstrained) length of a q contour.

---

[1] For the interest of the oceanographic community, we append a derivation of how one goes from Eq. (2) to (1), which parallels Walin's (1982) formulation of watermass transformation, as reviewed in Marshall et al. (1999). The theoretical frameworks of Nakamura (1996) and Walin (1982) are closely related to one another, although they were addressing rather different problems.

As discussed in more detail in section 3a, for Peclet number $Pe = (VL/k) \ll 1$, one would expect diffusion to dominate over advection, and hence K_{eff} to tend to k, with L_{eq} tending to L_{min}. However, if $Pe \gg 1$, then one might expect K_{eff} to be independent of the magnitude of k, because it is the stirring of tracers by the large-scale velocity field that controls the gradients of q on which the microscale diffusion acts. This has been shown to be true for the case of simple chaotic advection flows (Shuckburgh and Haynes 2003), and we will study whether it is also true for the oceanographic flows under consideration here. The action of diffusion is enhanced through differential advection, which, by the stretching and folding of material lines, produces small-scale structures in the tracer field. This is manifested by the enhancement of equivalent length L_{eq} over the minimum length L_{min}, resulting in an effective diffusivity that is larger than k [see Eq. (4)].

b. Solving the advection–diffusion tracer equation driven by altimetry

To apply the method described above we chose to focus on the Southern Ocean poleward of 30°S. Knowledge of surface diffusivities in the Southern Ocean is of great importance to understanding its dynamics and the role of eddy fluxes therein [see, e.g., Rintoul et al. (2001), Karsten and Marshall (2002), Marshall and Radko (2003), Olbers et al. (2004), and section 4a].

Altimetric observations over the Southern Ocean, taken every 10 days on a 1/4° latitude × 1/4° longitude grid, were used to provide the driving velocity field. Details of the altimetric data and the geoid model used in our study are given in the appendix. Before doing any serious calculations we began by inspecting movies of altimetric height. It was reassuring to observe the continuity of eddy features over time in the gridded data. For flows in a chaotic advection regime, it is the coarse-grained large-scale velocity field that is of the greatest import to tracer evolution and hence to calculation of effective diffusivity. Stratospheric flows appear to fall in this regime (e.g., Haynes and Shuckburgh 2000a,b), and there is some evidence that this is also true for surface-ocean flows (D. Waugh 2005, personal communication). This encouraged us to move on to directly implement our advection–diffusion problem driven by the evolving coarse-grained altimetric fields. First, the data were interpolated onto the higher-resolution grid on which the advection–diffusion calculation was carried out. The grids used at 1/20° and 1/100° are set in Table 1. The interpolated altimetric-derived velocity field was then made nondivergent, as is now described.

TABLE 1. Tabulated numerical values from our various tracer advection–diffusion calculations. Values of diagnosed K_{eff} are averages over the whole computational domain and so integrate out all spatial gradients; $Pe = (VL/k)$, $N_u = (K_{eff}/k)$, and $\delta = \sqrt{(k/S)}$, where $S = (V/L)$. Data from this table are plotted in the (N_u, Pe) plot in Fig. 3; the color coding used in the plot is indicated in the table.

Expt	Domain	Res (° lat)	k (m² s⁻¹)	K_{eff} (m²s⁻¹)	Pe	δ (km)	N_u
1	Global	$(1/20)°$ ($\equiv$5 km)	10	840	258	3.4	84
2	(43°–53°S)	”	25	1125	102	5.4	45
3	Orange dots	”	50	1280	52	7.7	26
4	”	”	100	1700	26	10.9	17
5	Patch I at (1/20)	$(1/20)°$ ($\equiv$5 km)	10	280	168	4.3	28
6	(43°–53°S), (43°–53°E)	”	100	630	17	13.5	6
	Green dots						
7	Patch I at (1/100)	$(1/100)°$ ($\equiv$1 km)	1	560	1763	1.3	557
8	(43°–53°S), (43°–53°E)	”	10	610	176	4.2	61
9	Dark blue dots	”	100	750	18	13.3	7
10	Patch II	$(1/20)°$ ($\equiv$5 km)	10	720	354	2.9	72
11	(30°–59°S), (40°–100°E)	”	50	1140	71	6.6	23
	Turquoise dots						
12	Patch III	$(1/20)°$ ($\equiv$5 km)	10	490	185	4.1	49
13	(38°–63°S), (105°–95°W)	”	25	690	74	6.5	28
14	Light turquoise dots	”	50	920	37	9.1	18
15	”	”	100	1260	19	12.9	13
16	”	”	500	2630	3.7	28.9	5.3
17	Global	$(1/4)°$ ($\equiv$25 km)	100	952	25	11.0	9.5
	(43°–53°S)						
	Yellow dot						

1) PREPARATION OF A NONDIVERGENT VELOCITY FIELD

If η is the altimetric height of the sea surface relative to the geoid, then the geostrophic relation yields the geostrophic current

$$\boldsymbol{v}_g = \frac{g}{f}\hat{\boldsymbol{z}} \times \boldsymbol{\nabla}\eta, \qquad (5)$$

where g is the acceleration due to gravity, $f = 2\Omega \sin \text{lat}$ is the Coriolis parameter, and $\hat{\boldsymbol{z}}$ is a unit vector in the vertical direction. Because of (i) variations in f and (ii) the presence of boundaries where the total normal velocity vanishes ($\boldsymbol{v} \cdot \mathbf{n} = \mathbf{0}$, where $\mathbf{n}$ is a unit vector normal to the boundary), Eq. (5) will yield a velocity field that is divergent. We therefore set

$$\boldsymbol{v} = \boldsymbol{v}_g + \boldsymbol{\nabla}\chi, \qquad (6)$$

where $\boldsymbol{\nabla}\chi$ is a (divergent) "adjustment" to the altimetric velocity that renders the sum $\boldsymbol{v}$ nondivergent, $\nabla \cdot \boldsymbol{v} = 0$. Thus, taking the horizontal divergence of Eq. (6), we obtain

$$\nabla^2\chi = -\boldsymbol{\nabla} \cdot \boldsymbol{v}_g, \qquad (7)$$

with boundary condition

$$\boldsymbol{\nabla}\chi \cdot \mathbf{n} = -\boldsymbol{v}_g \cdot \mathbf{n}. \qquad (8)$$

Thus the elliptic Eq. (7) was inverted for χ over the Southern Ocean with boundary conditions given by Eq.

(8) and the nondivergent velocity field was then constructed from Eq. (6).

The above calculations were carried out on the numerical grid on which the advection–diffusion problem was solved.

2) TIME STEPPING THE ADVECTION–DIFFUSION PROBLEM

Using a time series of nondivergent flow fields $\boldsymbol{v}$, generated according to the procedure laid out above, we advect a passive tracer q. The altimeter data yield one set of flow fields for each 10-day period. We calculate a set of 36 flow fields covering one annual cycle (from October 1996 until October 1997) and evolve q according to

$$\frac{\partial q}{\partial t} + \boldsymbol{v} \cdot \boldsymbol{\nabla}q = k\nabla^2 q. \qquad (9)$$

An initial distribution for q is chosen to align with the time-mean geostrophic streamlines as shown in Fig. 1a. This is to ensure that as the tracer evolves there is sufficient contrast in the tracer values between the different transport regions to allow a tracer-based coordinate system to be useful. One might add that rapid homogenization of tracer along streamlines is to be expected and that it is the cross-stream diffusivity that is required, and will be obtained here.
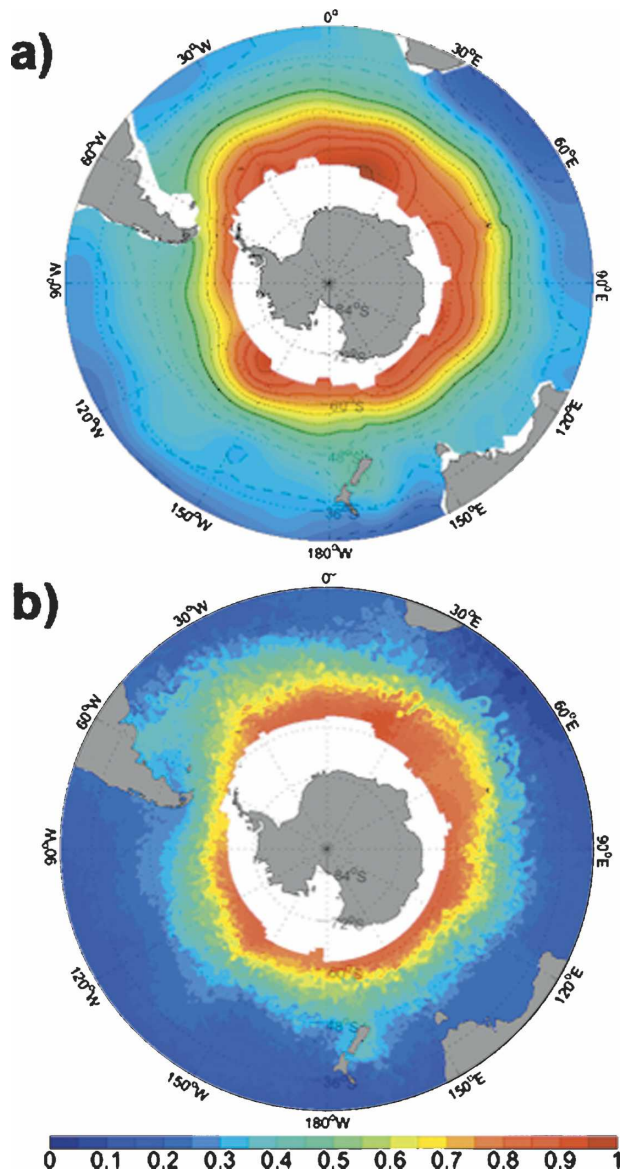
FIG. 1. (a) Time-mean geostrophic streamfunction Ψ_g (dotted contours are negative, contour interval 2×10^6 m^2 s^{-1}) and initial tracer distribution (colors). (b) Instantaneous tracer distribution, ranging in value from 0 to 1, after 1 yr of integration at 1/20° with $k = 50$ m^2 s^{-1}.

Equation (9) is stepped forward numerically on the sphere using the infrastructure of the Massachusetts Institute of Technology (MIT) general circulation model (Marshall et al. 1997). We choose to use an Adams–Bashforth time-stepping scheme in conjunction with a simple centered second-order discretization in space that conserves q and q^2 and introduces no spurious diffusion. We prefer not to use higher-order or "limited" schemes that, for example, conserve extrema, because they introduce diffusion that would compete with the

explicit process $k\nabla^2 q$, which is central to the Nakamura algorithm [see Eq. (3)].

Figure 1 shows (a) the initial tracer distribution and (b) the tracer after 1 yr of integration from a simulation at a $(1/20)°$ resolution with a diffusivity of $k = 50$ m^2 s^{-1}. A large number of such calculations were carried out, as set out in Table 1. Many are of subdomains—patches embedded in the larger-scale flow—and some are at a resolution as high as $(1/100)°$, which is much higher than was possible in the global domain. This enabled the explicit diffusivity to be reduced to low levels, allowing our calculations to span over a larger range of Pe. Figure 2 shows a number of patch calculations carried at different resolutions and with difference values of k, and hence Pe.

Because the velocity field is very smooth at small scales, a good description of the evolution of the q field is $q_t + Sxq_x = q_{xx}$, where $S = (V/L)$ is the strain rate, where V and L are typical scales for eddy speed and size. A balance between advection and diffusion occurs on the scale $\delta = \sqrt{(k/S)}$, a "Batchelor scale." The Pe number for these flows, comparing the advective time scale (L/V) with the diffusive time scale (L^2/k), is then Pe $= (VL/k) = (SL^2/k) = (L/\delta)^2$. From Table 1, we see that in our numerical experiments the Batchelor scale exceeds the grid spacing for all but the very smallest values of k used at the various resolutions. The results from such experiments must therefore be considered suspect.

The tracer field is extracted from the advection–diffusion simulation at regular time intervals and the effective diffusivity is calculated from it as described in the following section.

3. Estimates of surface eddy diffusivity

To compute K_{eff}, the gradient of the tracer is calculated at each grid point, and its square is integrated over the area bounded by the desired tracer contour. This integrated $|\nabla q|^2$ is then differentiated with respect to area by taking finite differences. The resulting quantity is then divided by the square of the areal gradient of the tracer to obtain $L_{eq}^2(q)$, as defined in Eq. (A5).

To obtain L_{min}^2 we take advantage of the fact that L_{eq} tends to L_{min} for Pe $\ll 1$. We therefore conduct an advection–diffusion integration with a large diffusivity k, which is chosen after sensitivity studies to be $k = 10^4$ m^2 s^{-1}, from which we estimate L_{min}. The effective diffusivity K_{eff} is then computed from Eq. (4).

There is an initial period of adjustment, lasting a few eddy turnover times, during which the initial tracer field adjusts to align with the flow. Following this adjustment time, the effective diffusivity remains approxi-
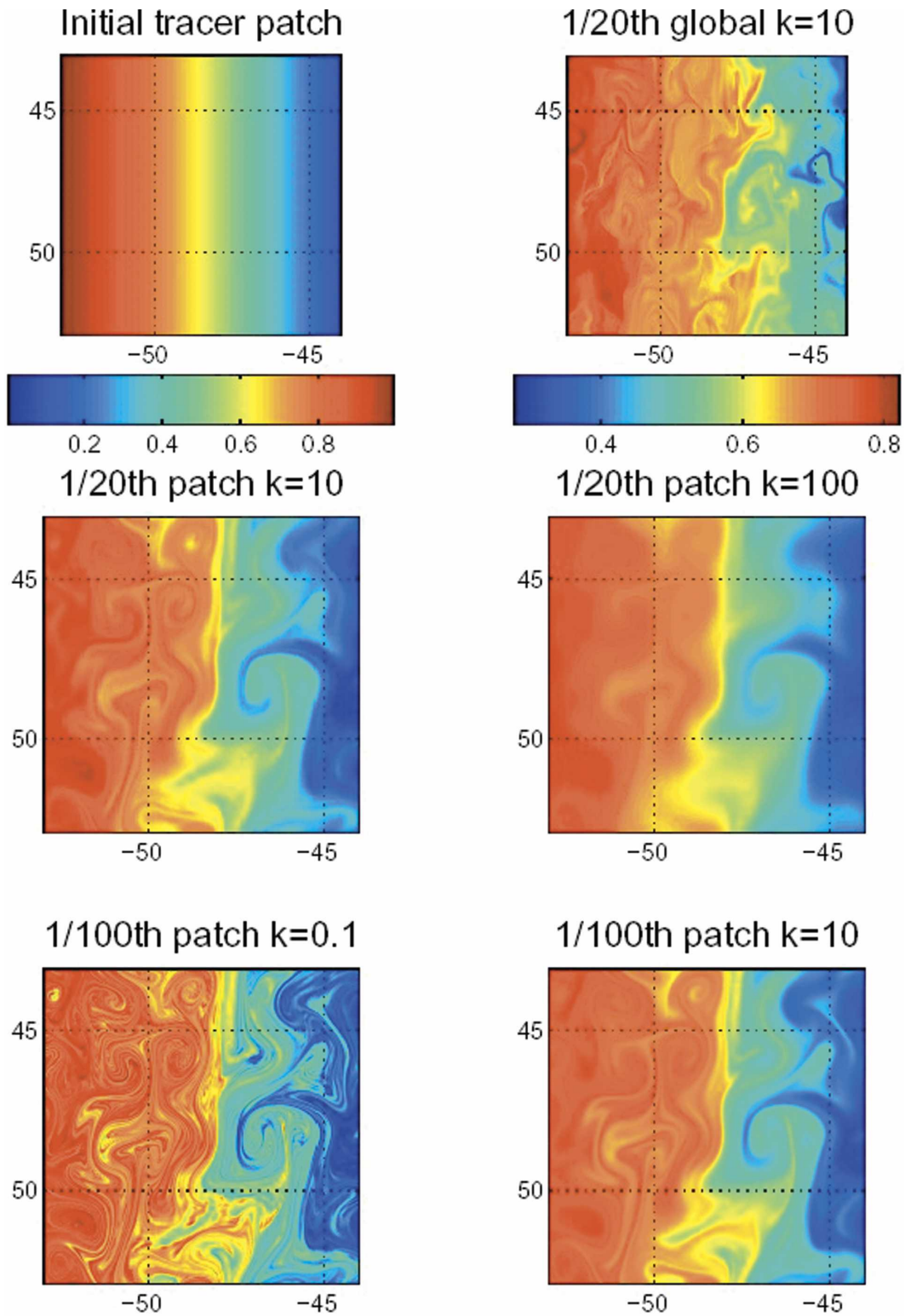
FIG. 2. Tracer distributions after 1 yr of integration carried out on a patch at various resolutions and diffusivities. The full suite of experiments is set out in Table 1.
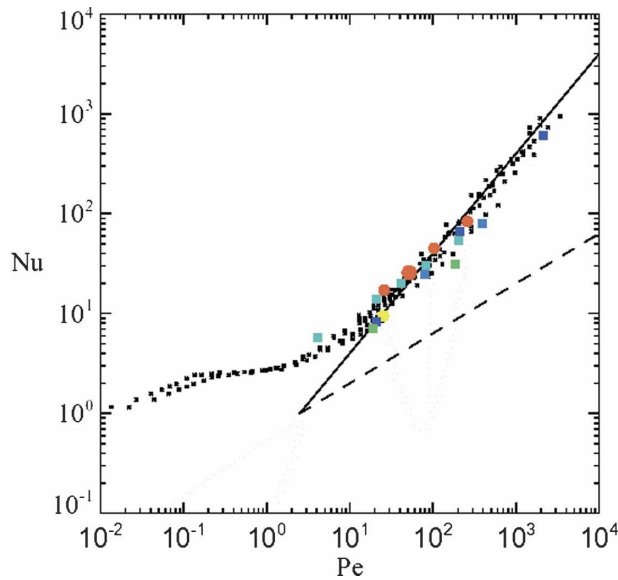
FIG. 3. Nusselt number based on the effective diffusivity $N_u = (K_{eff}/k)$ against a Peclet number based on the stretching rate $Pe = (VL/k)$. The continuous line has a slope of unity; the dotted line has a slope of one-half.

mately constant on each q contour, varying only to reflect changes in time of the velocity field. We will present the results of calculations representative of this postadjustment phase taken at 1 yr of integration, the time chosen to show the tracer distributions in Figs. 1 and 2.

a. Magnitude of K_{eff}

To study the dependence of our results on nondimensional parameters, in Fig. 3 we plot them all in (N_u, Pe) space, where $N_u = (K_{eff}/k)$ is a Nusselt number and $Pe = (SL^2/k)$ is the Peclet number, with $S \sim (V/L)$ calculated from a finite-time Lyapunov exponent calculation.[2] What might we expect the (N_u, Pe) plot to look like?

As discussed above, tracer stirring will create gradients on the Batchelor scale $\delta = \sqrt{(k/S)}$. The diffusive flux across filaments of scale δ will then be $F = (k\Delta q/\delta)$, where Δq is the jump in tracer value across the filament. But because $\Delta q = GL$, where G is the large-scale gradient and L is the eddy scale, then $F = (k/\delta)GL$.

There are two limit cases—when Pe is large and when it is small.

---

[2] We calculate finite-time Lyapunov exponents by following the separation of Lagrangian trajectories with initial perturbations of 10^{-6} in latitude and longitude and using the so-called "pull back" method to remove nonlinear effects resulting from amplification (see Shuckburgh and Haynes 2003).
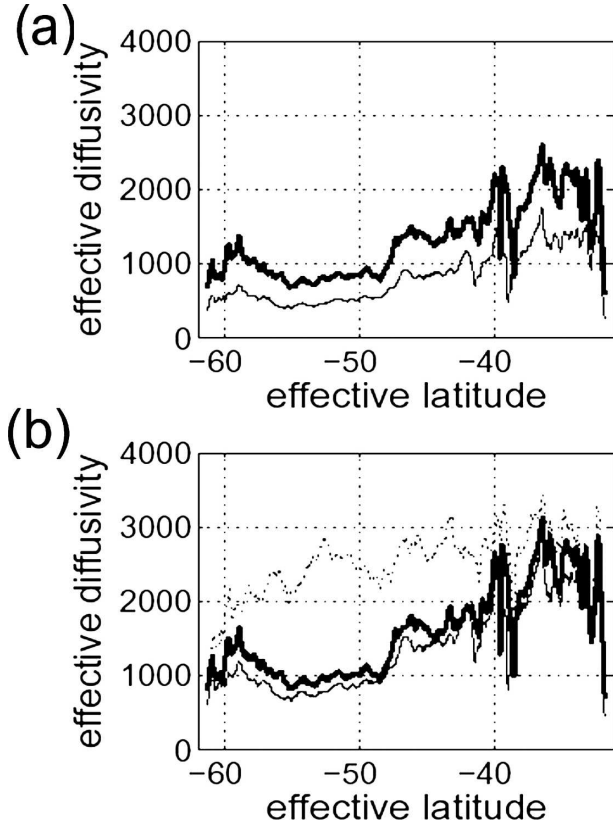
1) If Pe is large, the increase in the tracer gradient will be accompanied by an increase in the length of the tracer contours such that $L_{contour} \times \delta \sim L^2$ (ensuring that the area within a tracer contour is roughly conserved). Thus, the flux across the tracer contour will scale like $FL_{contour} = (k/\delta^2)L^3G = SL^3G = VL\Delta q$. We thus identify $K_{eff} \sim VL$, that is, independent of k. Hence, at large Pe the (N_u, Pe) should asymptotically approach a line of slope unity.

2) If Pe is small, then $L_{contour} \sim L$ and so $FL_{contour} = (k/\delta)L^2G = (k/\delta)L\Delta q = \sqrt{kVL}\Delta q$ and K_{eff} scales like $\sqrt{k}$. Hence, the line in the (N_u, Pe) plane would have a slope of ½.

The above scaling suggests that a line of slope unity in (N_u, Pe) space implies that K_{eff} is dependent only on the rate of straining of tracer gradients by the large-scale flow and is independent of small-scale mixing processes. A line of slope 0.5 suggests that the large-scale diffusive flux is set by processes right down on the Batchelor scale δ, that is, the rate-controlling process is diffusion across the filaments whose further scale collapse is inhibited by small-scale mixing k. The (N_u, Pe) plot in Fig. 3 includes, in black dots, the results for N_u and Pe taken from many chaotic advection calculations using a simple analytic flow (see Shuckburgh and Haynes 2003). These chaotic advection calculations congregate around a line with a slope that is just shy of unity, suggesting that K_{eff} for these flows is independent of k. The results of the altimetric-driven runs set in Table 1 are shown by the colored dots using quantities averaged over the domain of interest (the color code is given in the table). We see that these points all fall on lines with slopes that lie between 1 and 0.5. The best-fit line has a slope of 0.76, suggesting that $K_{eff} = k(Pe)^{0.76}$ and implying a K_{eff} that depends on $k^{0.24}$. Note that as Pe becomes smaller, one might expect N_u to approach unity, as indeed it does and must (because when explicit diffusion dominates, $K_{eff} \to k$).

Figure 4a shows K_{eff} plotted as a function of "equivalent latitude" for $k = 10$ m^2 s^{-1} and $k = 50$ m^2 s^{-1}. We see a very similar spatial variation of K_{eff} (discussed below), but values of K_{eff} are larger (by a factor of $\sim 5^{0.24} = 1.47$) for $k = 50$ m^2 s^{-1} than for $k = 10$ m^2 s^{-1}. From Fig. 3, it can be seen that as Pe becomes smaller the roll-off to a gently sloping line begins in the range $10 \lesssim Pe \lesssim 50$. From Table 1 we see that Pe ≈ 50 when $k \approx 50$ m^2 s^{-1}. Thus, at this rather high value of k we may indeed expect to observe some dependence of K_{eff} on k.

How large might k be expected to be in the mixed layer? Recent work (R. Ferrari et al. 2005, personal communication; see also Haine and Marshall 1998) sug-

FIG. 4. Results of a calculation of K_{eff} at $1/20°$ resolution plotted as a function of equivalent latitude for the cases with (a) $k = 50$ m^2 s^{-1}, indicated by the large red dot in Fig. 3 (thick line), and for $k = 10$ m^2 s^{-1} (thin line); (b) k_{num} [Eq. (10)] used instead of k in the calculation of K_{eff} for $k = 50$ m^2 s^{-1} (thick) and $k = 10$ m^2 s^{-1} (thin). Also plotted is K_{eff} from a calculation in which the tracer is advected only by eddies with the mean flow set to zero (dotted for $k = 50$ m^2 s^{-1}).

gests that buoyancy gradients enhanced by stirring through interior baroclinic instability are prone to nonhydrostatic instability of the mixed layer, which introduces a lateral mixing in the range of 10–100 m^2 s^{-1}. With these values of k, the Pe number is not particularly large (perhaps in the range 10–250), suggesting the mixed layer is in a regime in which K_{eff} is perhaps not independent of k. Indeed, it is in just this range of Pe number that points in (N_u, Pe) space tend to roll off the gradient 1 line in Fig. 3.

Another possibility is that the weak dependence of K_{eff} on k found here is of a numerical origin resulting from the use of second-order finite differences that generate noise on the grid scale, false extrema, small scales, and numerical dispersion.

The total numerical diffusivity will include both the explicit numerical diffusivity k and a contribution resulting from the numerical advection scheme. It may vary spatially, but an estimate of the average value (k_{num}) can be obtained by examining the decay with time of the globally averaged tracer variance (Allen and Nakamura 2001). Multiplying each side of Eq. (9), where k has been replaced by k_{num}, by q and taking the global average $\langle \rangle$, one obtains

$$\frac{1}{2}\frac{\partial\langle q^2\rangle}{\partial t} = -k_{num}\langle|\nabla q|^2\rangle. \qquad (10)$$

This equation can be used to estimate k_{num} by applying a regression analysis between the tendency of the tracer variance on the left-hand side and the mean squared tracer gradient on the right-hand side. For $k = 10$ m^2 s^{-1} and $k = 50$ m^2 s^{-1}, the estimated values of k_{num} from a best-fit calculation were found to be 17 and 60 m^2 s^{-1} respectively. From Fig. 4b it can be seen that the effective diffusivity is largely independent of the diffusivity when the total numerical diffusivity is used in the calculation.

Because the above analysis indicates that at $k = 50$ m^2 s^{-1} more than 80% of the total numerical diffusivity is accounted for by the explicit numerical diffusivity, in the remainder of this paper we choose to analyze in detail the results of our calculations at a resolution of $1/20°$ with $k = 50$ m^2 s^{-1}, indicated by the large red dot in Fig. 3.

b. Spatial variation of K_{eff}

From Fig. 4a it can be seen that K_{eff} takes a minimum value of around 750 m^2 s^{-1} at about $\phi_e = 55°$, with higher values on either side, reaching a maximum of about 2000 m^2 s^{-1} at about $\phi_e = 35°$.

The values of K_{eff} associated with each tracer contour q are plotted in Fig. 5a, with the mean streamlines overlaid. We have chosen not to plot the values of K_{eff} for tracer contours closest to the northern and southern boundaries because the calculation method can result in these values being spurious. It is important to note that $K_{eff}(\phi_e)$ represents an average value along a tracer contour q; the two-dimensional structure comes solely from the geometry of the tracer distribution q. Variations in the effective diffusivity along a tracer contour are not represented. For the purpose of this study we will be interested in the streamwise-averaged properties of the effective diffusivity for which the along-tracer variation will be of lesser importance. For studies of a particular geographical region, the effective diffusivity calculation should be repeated on a patch representing that geographical region alone, as in Fig. 2.

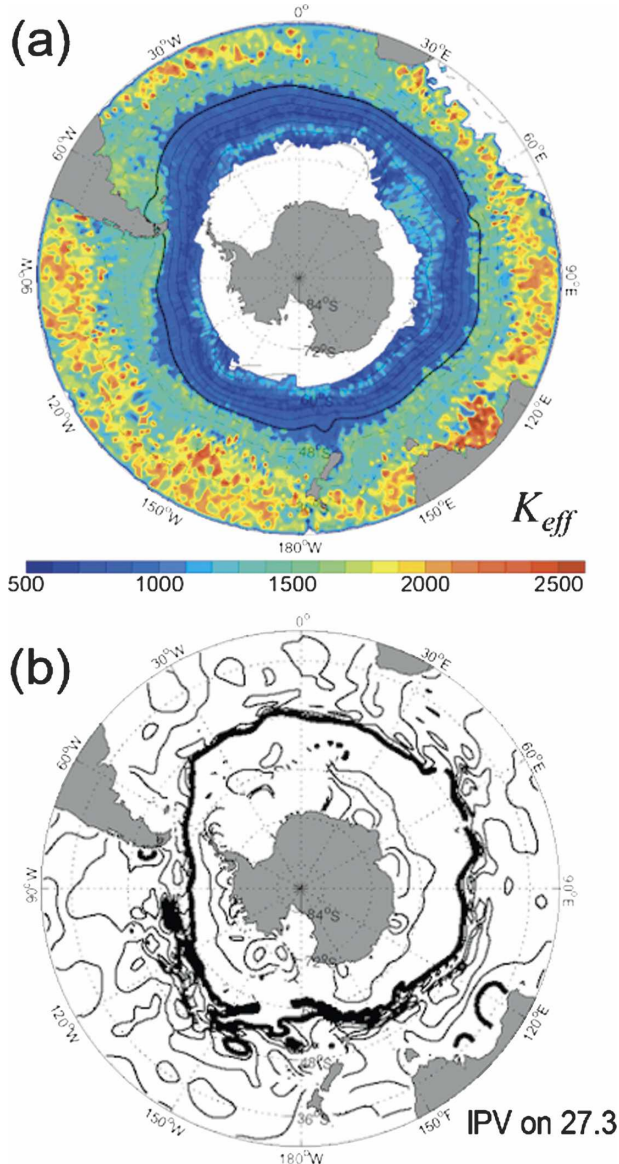From Fig. 5a it can be seen that the low values of eddy diffusivity ($K_{eff} < 1000$ m^2 s^{-1}, shown in dark

FIG. 5. (a) The $K_{eff}(q)$ for $k = 50$ m^2 s^{-1} plotted as a 2D map where q is the tracer distribution after 1 yr. The mean geostrophic streamline is superimposed. (b) The isentropic potential vorticity [$f(\partial\sigma/\partial z)$] distribution on the $\sigma = 27.3$ isopycnal surface normalized by a reference value. The thick contour marks the position of the front. The contour interval poleward of this line is 1 and the contour interval equatorward of it is 0.02. Details of the computation are given in Marshall et al. (1993).

blue) are closely associated with the ACC. Poleward of this jet there are slightly higher values of eddy diffusivity, and equatorward the values reach more than 2000 m^2 s^{-1} (orange/red). The magnitudes and geographical distribution of the diffusivities are consistent with those obtained using an adjoint model (see Fig. 12 of Ferreira et al. 2005) and those inferred by an inverse calculation (Olbers and Visbeck 2005). The pattern of weak eddy

diffusivities associated with a vortex edge or jet and stronger eddy diffusivities outside the vortex is seen repeatedly in geophysical flows, plasma physics, and simple analytic flows, as discussed in Shuckburgh and Haynes (2003). One prominent example is the stratospheric polar vortex, which is characterized by a strong barrier near the core of the jet and a "surf zone" of strong eddy mixing equatorward of this. The barrier effect is thought to be a consequence of the quasi-elastic resilience engendered by the strong potential vorticity gradients at the vortex edge (see Juckes and McIntyre 1987). The strong mixing is thought to be associated with Rossby wave breaking near the critical layer (where the phase speed of the wave $c = \bar{u}$, the mean zonal flow; see Haynes 1985), eroding PV gradients. In support of this conjecture, in Fig. 5b we plot the observed isentropic potential vorticity (IPV) distribution [$f(\partial\sigma/\partial z)$] on the $\sigma = 27.3$ isopycnal surface (details of the computation are given in section 4 of Marshall et al. 1993). A striking feature is the collar of high PV resulting from very stable stratification around the pole, a sharp PV gradient roughly coincident with the core of the ACC, and much smaller values of PV in a broad region on the equatorial flank. Indeed, the PV field here on the equatorial flank is remarkably uniform with very weak PV gradients. The regions of high eddy diffusivity coincide with those of weak PV gradients, and regions of low diffusivity with high PV gradients (cf. Fig. 5a with Fig. 5b). One is reminded of float observations in the Gulf Stream discussed by Bower et al. (1985), which suggest that the barrier effect could be stronger at the surface than at middepth. Indeed, it is likely that there may be a complex vertical structure to the diffusivity.

As discussed above, the broad patterns of the meridional structure of K_{eff} can be rationalized in terms of the large-scale flow structure. The dotted line in Fig. 4b also draws out the importance of the mean flow structure on $K_{eff}(q)$ by demonstrating that in the absence of a jet at the latitude of the ACC uniformly high values are obtained throughout the domain.

4. Implications of new estimates of K for Southern Ocean dynamics

a. The Deacon cell of the Southern Ocean

What inferences can we draw from our K_{eff} distributions about the role of eddies in the dynamics of the Antarctic Circumpolar Current? Because of the absence of zonal pressure gradients in the ACC, eddies must play a central role in momentum and buoyancy budgets, see, for example, the review by Rintoul et al.

(2001) and the theoretical model of Marshall and Radko (2003).

Taking a streamwise average of the along-stream residual momentum equation in the planetary geostrophic limit [see Eq. (A7) and the discussion in the appendix] the pressure gradient term vanishes on those contours that circumnavigate the globe, and we obtain

$$-f\bar{v}_{\mathrm{res}} = \frac{1}{\rho_{\mathrm{ref}}} \frac{\partial(\bar{\tau}_x^w + \bar{\tau}_x^e)}{\partial z}. \tag{11}$$

Here the overbars represent a temporal and streamwise average, $\bar{v}_{\mathrm{res}}$ is understood to be the residual current normal to the mean surface streamlines, and $\bar{\tau}_x^e$ is the streamwise average of the zonal eddy stress given by Eqs. (A11) and (A13) of the appendix. Integrating down from the surface, where $\tau^w = \tau_{x_{\mathrm{wind}}}$ is the zonal surface wind stress and the eddy stress is $\tau^e = 0$, to the bottom of the diabatic layer at depth h_s, where $\tau^w = 0$ and τ_x^e is given by Eqs. (A11) and (A13), we find, using $v_{\mathrm{res}} = -(\partial \psi_{\mathrm{res}}/\partial z)$ with $\psi_{\mathrm{res}} = 0$ at $z = 0$,

$$\psi_{\mathrm{res}_{z=-h_s}} = \underbrace{-\frac{\bar{\tau}_{x_{\mathrm{wind}}}}{\rho_{\mathrm{ref}} f}}_{\psi^{\mathrm{Eu}}} + \underbrace{\left(\frac{\overline{v'b'}}{\bar{b}_z}\right)_{z=-h_s}}_{\psi^*}. \tag{12}$$

We see that ψ_{res} at the bottom of the diabatic layer is made up of an Eulerian-mean contribution resulting from the Ekman layer (ψ^{Eu}) and an eddy-induced contribution resulting from the lateral eddy buoyancy fluxes (ψ^*).

In the nomenclature of Speer et al. (2000), we can call ψ^{Eu} the Deacon cell (after Deacon 1937) and ψ_{res} the diabatic Deacon cell. The Deacon cell can be inferred from the wind stress shown in Fig. 6. The zonal wind stress is strong and persistent around the Southern Ocean reaching, when averaged along mean streamlines, a maximum of some 0.14 N m^{-2} just on the equatorward flank of the ACC. Three different climatologies are presented to give an impression of the uncertainty in these estimates. Although there are considerable differences, a broad pattern emerges. Figure 7 shows ψ^{Eu} deduced by simply averaging the three datasets (assuming that none is superior to another), integrating along mean streamlines, and dividing by the Coriolis parameter f. We see that ψ^{Eu} reaches a magnitude of some 30 Sv (Sv $\equiv 10^6$ m^3 s^{-1}) at 50°S, with surface flow directed away from Antarctica.

We can estimate the residual flow as follows. As shown in Marshall (1997) and applied in Speer et al.
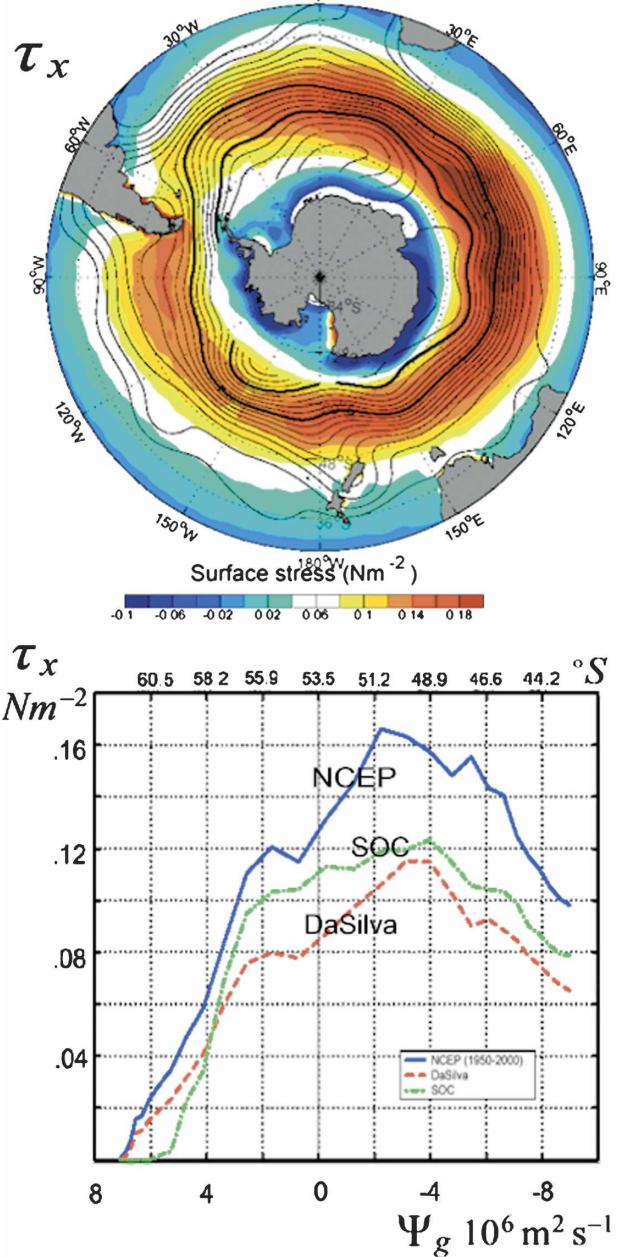

FIG. 6. (top) The mean zonal wind stress for the period 1980–2000 from the National Centers for Environmental Prediction (NCEP) reanalysis (N m^{-2}). (bottom) The streamwise-averaged wind stress computed from (i) NCEP (ii) Southampton, United Kingdom, and (iii) the Da Silva et al. (1994) reanalysis products plotted against the mean geostrophic streamfunction (Ψ_g). The mean latitude of the mean streamfunction is also indicated.

(2000) and Marshall and Radko (2003), $\psi_{\mathrm{res}_{z=-h_s}}$ can be inferred from the buoyancy budget of the mixed layer; thus,

$$\psi_{\mathrm{res}_{z=-h_s}} = \frac{\tilde{B}}{\bar{b}_y}, \tag{13}$$
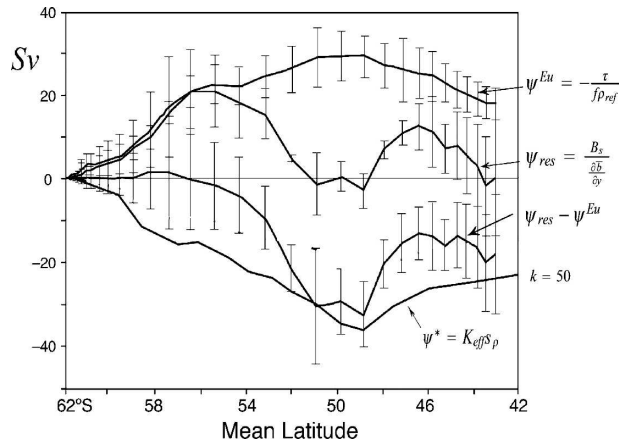
FIG. 7. Estimates of the streamwise-averaged values of (i) ψ^{Eu} from Eq. (12) using the three analyzed fields of surface stress shown in Fig. 6 (error bars represent $\pm$ one std dev, assuming that none of the three wind stress products is superior to any other); (ii) ψ_{res} deduced using Eq. (13) from analyzed fields of surface buoyancy fluxes and a WOCE climatology to obtain $\bar{b}$; (iii) the difference $\psi_{\mathrm{res}} - \psi^{\mathrm{Eu}}$; and (iv) ψ^* from Eq. (14) using our estimates of K_{eff} and observation of isopycnal slope at the base of the diabatic layer h_s.
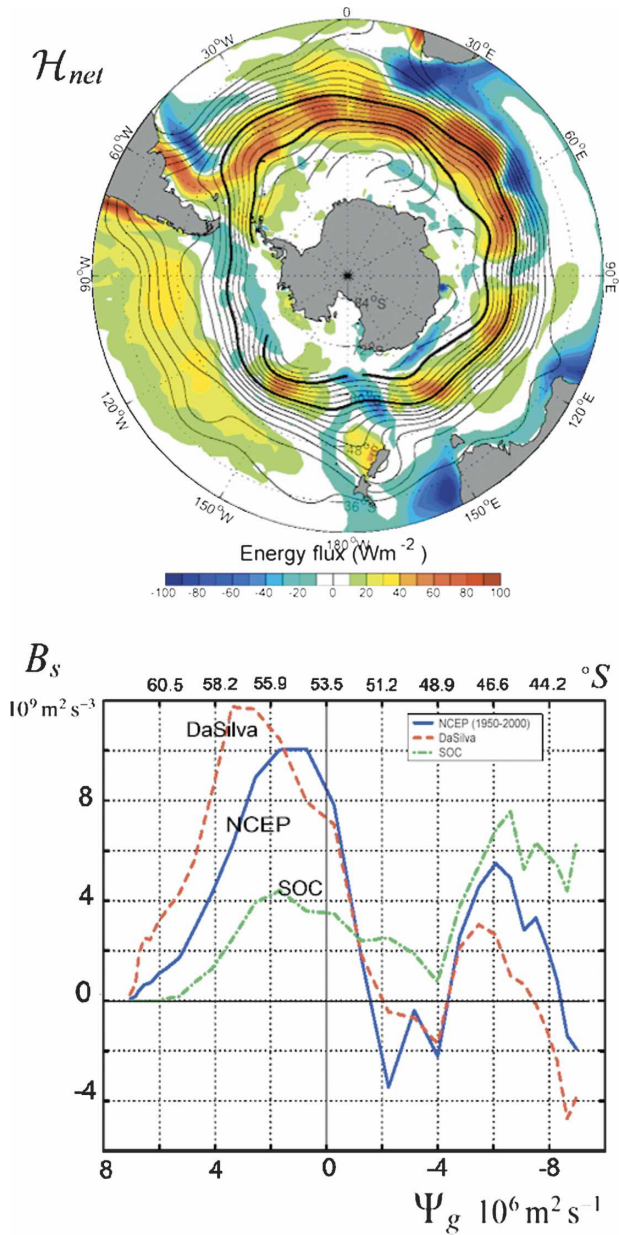

FIG. 8. (top) The mean net air–sea heat flux for the period 1980–2000 from the NCEP reanalysis (N m^{-2}) Blue indicates regions where the heat flux is out of the ocean, and yellow-orange represents regions where it is directed in to the ocean. (bottom) The streamwise-averaged mean net air–sea heat flux computed from (i) NCEP, (ii) Southampton, and (iii) the Da Silva et al. (1994) reanalysis products plotted against the mean geostrophic streamfunction (Ψ_g). The mean latitude of the mean streamfunction is also indicated.

where $\tilde{B}$ is the net buoyancy forcing of the mixed layer [including the contribution of diabatic eddy fluxes, see Eq. (12) of Marshall and Radko (2003) and the definition of F_{res} in the appendix] and $\bar{b}_y$ is the meridional buoyancy gradient at the base of the mixed layer. Figure 8 shows three estimates of the air–sea buoyancy flux. The difference between them is even larger than for the surface wind stress, perhaps because of uncertainties in estimates of evaporation and precipitation ($E - P$). Nevertheless, again a consistent broad pattern emerges. On the axis and spreading poleward of the ACC there is buoyancy flux in the ocean; just equatorward of the ACC, the flux is much smaller in magnitude and, if anything, is directed out of the ocean. The geographical distribution of the broad patterns of air–sea heat flux (the largest contributor to the air–sea buoyancy flux) can be seen in the top panel of Fig. 8, where the yellow/orange regions indicate heat flux into the ocean, and the blue regions indicate heat flux out of the ocean. The streamwise-averaged ψ_{res} computed from Eq. (13) [evaluated using $\bar{b}_y$ at the base of the mixed layer computed from a gridded World Ocean Circulation Experiment (WOCE) climatology resulting from Gouretski and Jancke (1998)] is one of the curves shown in Fig. 7. Note that here we have set $\tilde{B} = B_s$, the net air–sea buoyancy flux, and neglected lateral eddy contributions (F_{res}) to $\tilde{B}$. We see that our estimate of ψ_{res} is markedly different from that of ψ^{Eu}, being considerably smaller in magnitude and exhibiting much more meridional structure. The ψ_{res} pattern suggests

the upwelling of fluid poleward of 56°S of some 20 Sv and downwelling of the same fluid magnitude between 56° and 50°S, not inconsistent with other estimates (see, e.g., Karsten and Marshall 2002).

Also plotted in Fig. 7 is the difference $\psi_{\mathrm{res}} - \psi^{\mathrm{Eu}}$,

which [see Eq. (12)] can be identified with the eddy-induced streamfunction $\Psi*$.[3] If eddies are to substantially balance ψ^{Eu} they must achieve a poleward volume transport of some 30 Sv. We can use our estimate of K_{eff} to see whether this is possible or likely.

In Fig. 7 we therefore also plot the streamwise average of the x component of Eq. (A13),

$$\Psi* = \frac{\overline{v'b'}}{\overline{b}_z} = K_{eff}s_\rho, \qquad (14)$$

where $s_\rho = -(\overline{b}_y/\overline{b}_z)$ is the isopycnal slope at the base of the mixed layer as computed from the WOCE climatology of Gouretski and Jancke (1998). It is very encouraging to observe that $\Psi*$ tracks $\Psi_{res} - \psi^{Eu}$ rather closely, lending strong support to the idea that transient eddies are playing an order of one role in balances in the Southern Ocean. Note that in the limit that $\psi_{res} \to 0$, the eddy stress exactly balances the wind stress.

b. Maps of eddy stresses in the Southern Ocean

An appealing way of assessing the importance of transient eddy processes in Southern Ocean dynamics is to again adopt a "residual mean" perspective and use our effective diffusivity to compute the zonal eddy stress, given by [see Eqs. (A11) and (A13)] $\tau_x^e = \rho_{ref}fK_{eff}s_\rho$, and compare it with the surface wind stress.

The zonal stress so computed is plotted in Fig. 9 in units of N m^{-2}. We see that over the axis of the ACC it is comparable in strength to that of the surface wind stress (cf. with Fig. 6). One should remember the asymmetry between τ_x^e and τ_x^w. The absolute value of the eddy stress initially always increases in magnitude with depth from zero at surface. Given that typically $\tau_x^e > 0$ along the path of the ACC, this drives, via Eq. (11), surface eddy-induced circulation toward the pole, as sketched in the schematic diagram in Fig. 10. In contrast, the absolute value of τ_x^w decreases in magnitude with depth. Along the path of the ACC $\tau_x^w > 0$, but now an equatorward Ekman flow is driven, also sketched in Fig. 10. We thus again clearly see the opposing nature of the wind- and eddy-forced ageostrophic residual flow in the surface layers of the ACC.

5. Conclusions and discussion

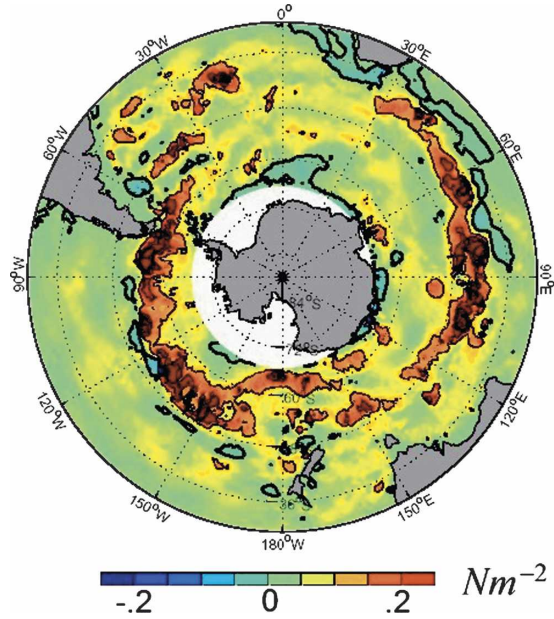We have inferred effective diffusivities by numerically monitoring the lengthening of tracer contours [Eq.

FIG. 9. The zonal component of eddy stress (N m^{-2}) computed from $\tau_x^e = \rho_{ref}fK_{eff}s_\rho$ using our estimate of K_{eff} (Fig. 4a), using the $k = 50$ curve.

(4)] as they are strained by surface geostrophic flow in the Southern Ocean observed by satellite altimetry. The theoretical background to the calculation is that resulting from Nakamura (1996). It is reviewed in an appendix where connections are made to the Walin (1982) formulation of watermass transformation.

The following broad conclusions can be drawn, which, we feel, will stand the test of time and transcend
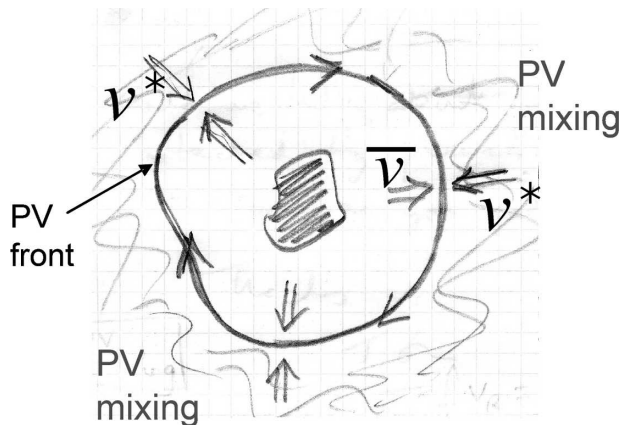

FIG. 10. The ACC flows along a front in the large-scale IPV field. Eddy stresses drive surface flow poleward toward the axis of the ACC and wind stresses drive surface flow equatorward. Surface convergence and subsequent subduction can thus be expected to take place in the vicinity of the axis of the ACC, with the exact location depending on the relative magnitude of the eddy stresses and wind stresses.

the particular methods and implementation details used in our study:

1) Effective diffusivities associated with the lateral stirring of properties at the sea surface resulting from interior baroclinic instability show considerable spatial variability, by a factor of at least 2, and are large on the equatorward flank of the ACC and are small at the jet axis (see Fig. 4). This signature is a very robust result and is not sensitive to numerical details.

2) We expect, and indeed observe, that regions of high and low effective diffusivity are collocated with regions of, respectively, weak and strong isentropic PV gradients. This is a common feature of geophysical flows. In regions of high diffusivity, one might expect PV gradients to be eroded; regions of low diffusivity might be associated with the transport barrier effects of strong PV gradients. However, the focus here has been on near-surface diffusivities; the vertical structure of the diffusivity needs to be mapped out, perhaps using the tracer advection techniques discussed here.

3) Eddy stresses drive surface residual flow toward the pole and wind stresses drive surface residual surface fluid away from the pole, as sketched in Fig. 10. Surface convergence and subsequent subduction can thus be expected to take place in the general vicinity of the ACC, with the exact location depending on the relative magnitude of the eddy stresses and wind stresses.

4) In the 10–250 Pe number range employed in the present study (see Fig. 3) absolute magnitudes of effective diffusivity are found to be somewhat dependent on the magnitude of the microdiffusivity used to calculate them using Eq. (4), although much less so than when the full numerical diffusivity is accounted for. A dependency on k could perhaps be interpreted in the context of a real physical process, for example, the small-scale diffusivity associated with baroclinic instability local to the mixed layer acting on surface buoyancy gradients created by straining of surface properties by the interior geostrophic eddy field. We find that effective diffusivities range in magnitude across the ACC from 2000 to 500 $m^2\,s^{-1}$ (see Fig. 4).

5) For the aforementioned range of effective diffusivities, eddy stresses are comparable in magnitude to wind stresses (see Fig. 9), suggesting that eddy processes play a zero-order role in the streamwise-averaged dynamics of the ACC.

APPENDIX

Data and Theory

a. TOPEX data

The time series of altimetric observations are sea level anomaly (SLA) maps obtained from the final combined processing of Ocean Topography Experiment (TOPEX)/Poseidon (T/P) and *European Remote Sensing Satellite* (*ERS*)-*1/2* data. There is one map every 10 days for a period of 5 yr (from October 1992 to October 1997). Anomaly maps were obtained using an improved space–time objective analysis method, which takes into account long wavelength error correlated noise. The method is described in Le Traon et al. (1998). For each grid point, data inside a time window of ±10 days for T/P and ±18 days for ERS, and a space window of ±3 ZC, are used. The maps have a resolution of 0.25° × 0.25°.

Sea level anomalies are relative to a 3-yr mean (from January 1993 to January 1996). Specific processing is performed to obtain an *ERS-1/2* mean that is consistent with T/P mean. The TOPEX/Poseidon merged geophysical data record (M-GDR; version C) recently reprocessed by the Archiving, Validation, and Interpretation of Satellite Oceanographic Data Center (AVISO) was used. This version includes, in particular, the new Joint Gravity Model (JGM-3) orbits, the Center for Space Research (CSR3.0) tidal model, and the correction of TOPEX drift. *ERS-1/2* are the ERS Ocean Products (OPRs) distributed by the Centre d'étude et de Recherche en Géodynamique et Astrométrie (CERSAT). Altimetric corrections were updated to be homogenous with T/P, and a global adjustment using T/P as a reference was performed to correct for *ERS-1/2* orbit error. Additional information can be found in Le Traon and Ogor (1998).

The height relative to the geoid is obtained by subtracting the geoid model described in Lemoine et al. (1997).

b. Derivation of K_{eff} formulas

To make contact points between the meteorological and oceanographic literature we review and derive Nakamura's (1996) expression Eq. (3), beginning from the watermass transformation formalism resulting from
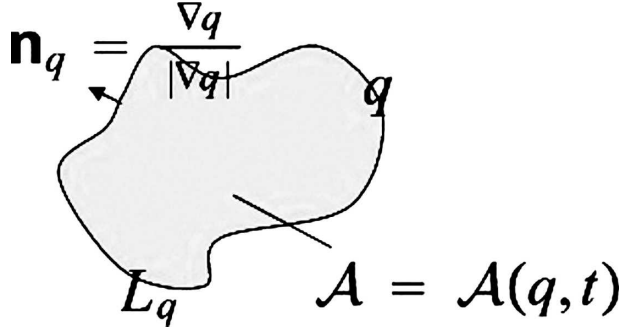
FIG. A1. A tracer contour q demarcating an area $A(q, t)$. The outward normal to the q contour is n_q.

Walin (1982). Our starting point is the tracer advection equation [Eq. (2)], which we write in the form

$$\frac{\partial q}{\partial t} = -\nabla \cdot (\mathbf{N}_q + q\mathbf{v}),$$

where $\mathbf{N}_q$ is the nonadvective (diffusive) flux of q

$$\mathbf{N}_q = -k\nabla q. \tag{A1}$$

The volume flux across q contours, defined by

$$a = \oint (\mathbf{v} - \mathbf{v}_q) \cdot \mathbf{n}_q \, dl,$$

where $\mathbf{n}_q = (\nabla q / |\nabla q|)$ is a unit vector normal to q contours and $\mathbf{v}_q = (\mathbf{n}_q / |\nabla q|)(\partial q / \partial t)$ is the velocity of a q contour normal to itself, can only be associated with nonadvective fluxes (because the advecting velocity field is nondivergent; see Fig. A1). This volume flux can be related to diffusive fluxes as follows [see Garrett and Tandon 1997; Marshall et al. 1999, their Eq. (3.7)]:

$$a = \frac{\partial A}{\partial t} = -\frac{\partial D}{\partial q}, \tag{A2}$$

where D is the diffusive flux across a q contour given by[A1]

$$D = \oint \mathbf{N}_q \cdot \mathbf{n}_q \, dl = \oint \mathbf{N}_q \cdot \frac{\nabla q}{|\nabla q|} \, dl = \frac{\partial}{\partial q} \int \mathbf{N}_q \cdot \nabla q \, dA.$$

For an $\mathbf{N}_q$ given by Eq. (A1), then

$$D = -k \frac{\partial}{\partial q} \int |\nabla q|^2 dA,$$

and Eq. (A2) becomes

$$\frac{\partial A}{\partial t} = -\frac{\partial D}{\partial q} = k \frac{\partial}{\partial q} \frac{\partial}{\partial q} \int |\nabla q|^2 \, dA.$$

Now, because $A = A(q)$, then $(\partial A/\partial t) = (\partial A/\partial q)(\partial q/\partial t)$; $(\partial/\partial q) = (\partial A/\partial q)(\partial/\partial A)$ and the above may be written as a diffusion equation in area coordinates, thus,

$$\frac{\partial q}{\partial t} = \frac{\partial}{\partial A}\left[\kappa_{\text{eff}}(A) \frac{\partial q}{\partial A}\right], \tag{A3}$$

with diffusion coefficient

$$\kappa_{\text{eff}}(A) = k \frac{1}{\left(\frac{\partial q}{\partial A}\right)^2} \frac{\partial}{\partial A} \int_{A(q,t)} |\nabla q|^2 \, dA. \tag{A4}$$

Thus, q diffuses in A coordinates at rate κ_{eff}, which, according to Eq. (A4), can be computed by summing up $|\nabla q|^2$ between adjacent q contours.

Rhines and Young (1983) consider the dispersion of a tracer in steady 2D flow. They give an explicit expression for the diffusivity across each streamline in the limit of small diffusivity. Nakamura and Ma (1997) note that, in the same limit, this cross-stream diffusivity is equal to the corresponding effective diffusivity. Note, however, that Eqs. (A3) and (A4) are more general than the special case of steady 2D flow considered in Rhines and Young (1983).

The effective diffusivity can be related to the length of q contours strained by the velocity field, as can be seen as follows. Note that κ_{eff} has units of meters to the fourth power per second, that is, that of diffusivity $\times$ length^2; the diffusivity in area coordinates is [see Eq. (A4)] kL_{eq}^2, where L_{eq}, known as the equivalent length, is given by

$$L_{\text{eq}}^2 = \left(\frac{\partial A}{\partial q}\right)^2 \frac{\partial}{\partial A} \int |\nabla q|^2 \, dA = \underbrace{\frac{\partial A}{\partial q} \frac{\partial}{\partial q}}_{\frac{\partial A}{\partial q}\frac{\partial}{\partial A}} \int |\nabla q|^2 \underbrace{\frac{dl \, dq}{|\nabla q|}}_{dA} = \underbrace{\oint \frac{dl}{|\nabla q|}}_{\frac{\partial A}{\partial q}} \oint |\nabla q| \, dl, \tag{A5}$$

where we have used the relation $(\partial A/\partial q) = (\partial/\partial q)\int dA = (\partial/\partial q)\int(dl\,dq/|\nabla q|) = \oint(dl/|\nabla q|)$.

Because $L = \oint dl$, then $L_{\text{eq}}^2 = L^2$, the actual length of a q contour, if $|\nabla q| = \text{const}$ on dl. If $|\nabla q| \neq \text{const}$ on dl, then $L_{\text{eq}}^2 \geq L^2$, as discussed in Haynes and Shuckburgh (2000a). This can be seen as follows. Writing $L = \oint |\nabla q|(dl/|\nabla q|) = (\partial/\partial q)\int |\nabla q| \, dA = [1/(\partial q/\partial A)](\partial/\partial A)\int |\nabla q| \, dA$ we see that

---

[A1] The following identity (a generalized form of Leibnitz theorem) is used: $(\partial/\partial q)\int_A c(\mathbf{x}, t) \, dA = \oint_L c(\mathbf{x}, t)|\nabla q|^{-1} \, dl$.

$$L_{eq}^2 = \frac{1}{\left(\frac{\partial q}{\partial \mathcal{A}}\right)^2} \frac{\partial}{\partial \mathcal{A}} \int |\nabla q|^2 \, d\mathcal{A} \geq L^2$$

$$= \left[\frac{1}{\left(\frac{\partial q}{\partial \mathcal{A}}\right)} \frac{\partial}{\partial \mathcal{A}} \int_{\mathcal{A}} |\nabla q| \, d\mathcal{A} \right]^2,$$

because the "sum of the squares" is always greater than "the square of the sum."

To obtain diffusivity with conventional units we define a quantity

$$K_{eff} = \frac{kL_{eq}^2}{L_{min}^2}, \qquad (A6)$$

where L_{min} is the minimum length of a q contour. Because $L_{eq}^2 \geq L^2 \geq L_{min}^2$, geometrically κ_{eff} may be interpreted as the enhancement of diffusion resulting from the enhanced complexity of the tracer contours. On a sphere, the minimum length of a tracer contour is given by $L_{min} = 2\pi r \cos\phi_e$, where ϕ_e is known as the "equivalent latitude," this being the slowest decaying mode of the diffusion equation on a sphere. For application to the Southern Ocean, the continental boundaries prevent this minimum state from being reached and the slowest decaying mode of the diffusion equation is not given by a simple analytic formula. We therefore obtain L_{min} numerically.

c. Residual-mean theory

The residual momentum equation can be written in the planetary geostrophic limit (see, Ferreira et al. 2005) as follows:

$$f\hat{z} \times \boldsymbol{v}_{res} = -\frac{1}{\rho_{ref}} \nabla p + \frac{1}{\rho_{ref}} \frac{\partial (\boldsymbol{\tau}^w + \boldsymbol{\tau}^e)}{\partial z}, \qquad (A7)$$

where $\boldsymbol{v}_{res}$ is the residual flow, the sum of mean and eddy contributions,

$$\boldsymbol{v}_{res} = \overline{\boldsymbol{v}} + \boldsymbol{v}^*, \qquad (A8)$$

and the eddy-induced velocity $\boldsymbol{v}^*$ can be expressed in terms of a vector streamfunction as follows:

$$\boldsymbol{v}^* = -\nabla \times \boldsymbol{\Psi}, \qquad (A9)$$

defined by

$$\boldsymbol{\Psi} = (\Psi_x, \Psi_y) = \left(\frac{\overline{v'b'}}{\overline{b}_z}, -\frac{\overline{u'b'}}{\overline{b}_z}, 0 \right). \qquad (A10)$$

The eddy stress is related to the eddy streamfunction, thus,

$$\boldsymbol{\tau}^e = (\tau_x^e, \tau_y^e) = \rho_{ref} f \boldsymbol{\Psi}, \qquad (A11)$$

where $\boldsymbol{\Psi}$ is given by Eq. (A10).

The associated residual-mean buoyancy equation is

$$\frac{\partial \overline{b}}{\partial t} + \boldsymbol{v}_{res} \cdot \nabla \overline{b} = -\nabla \cdot \mathbf{F}_{res} + S, \qquad (A12)$$

where S is the diabatic source and sink and $\mathbf{F}_{res} = (\overline{v'b'} \cdot \nabla \overline{b}/\overline{b}_z)\hat{z}$ is the residual eddy flux with $\hat{z}$ a unit vector in the vertical direction.

Complications arise near boundaries. Following Treguier et al. (1997), the domain is divided into an adiabatic interior where the eddy flux is skew ($\mathbf{F}_{res} \rightarrow 0$) and a surface layer of depth h_s where eddy fluxes develop a diabatic component as they become parallel to the boundary and isopycnal surfaces steepen under the influence of turbulent mixing and air–sea fluxes. In this surface layer the definition of $\boldsymbol{\Psi}$ is modified by assuming that the return flow is spread over the diabatic layer

$$\boldsymbol{\Psi}_{z=-h_s} = \left(\frac{\overline{v'b'}}{\overline{b}_z}, -\frac{\overline{u'b'}}{\overline{b}_z}, 0 \right)_{z=-h_s} \mu, \quad -h_s < z < 0,$$

$$(A13)$$

where μ changes from 0 at the surface to 1 at $z = -h_s$. This ensures that $\boldsymbol{\Psi} = 0$ and hence that $\boldsymbol{\tau}^e = 0$ on the boundary.

REFERENCES

Allen, D. R., and N. Nakamura, 2001: A seasonal climatology of effective diffusivity in the stratosphere. *J. Geophys. Res.,* **106** (D8), 7917–7935.

Batchelor, G. K., 1959: Small-scale variation of convected quantities like temperature in a turbulent fluid. Part 1. General discussion and the case of small conductivity. *J. Fluid Mech.,* **5,** 113–133.

Bower, A. S., H. T. Rossby, and J. L. Lillibridge, 1985: The Gulf Stream—Barrier or blender? *J. Phys. Oceanogr.,* **15,** 24–32.

Bryden, H. L., and R. A. Heath, 1985: Energetic eddies at the northern edge of the Antarctic Circumpolar Current. *Progress in Oceanography*, Vol. 14, Pergamon, 65–87.

Da Silva, A. M., C. C. Young, and S. Levitus, 1994: *Algorithms and Procedures.* Vol. 1, *Atlas of Surface Marine Data 1994,* NOAA Atlas NESDIS 6, 74 pp.

Davis, R. E., 1991: Observing the general circulation with floats. *Deep-Sea Res.,* **38A** (Suppl. 1), S531–S571.

Deacon, G. E. R., 1937: The hydrology of the southern ocean. Discovery Rep. 15, 1–124.

Deese, H. E., L. J. Pratt, and K. R. Helfrich, 2002: A laboratory model of exchange and mixing between western boundary layers and sub-basin recirculation gyres. *J. Phys. Oceanogr.,* **32,** 1870–1889.

Ferreira, D., J. Marshall, and P. Heimbach, 2005: Estimating eddy stresses by fitting dynamics to observations using a residual-mean ocean circulation model. *J. Phys. Oceanogr.,* **35,** 1891–1910.

Garrett, C., and A. Tandon, 1997: The effect of water mass transformation on surface mixed layer time-dependence and entrainment fluxes. *Deep-Sea Res. I,* **44,** 1991–2006.

Gouretski, V. V., and K. Jancke, 1998: A new climatology for the

World Ocean. WOCE Special Analysis Centre, Max-Planck Institut, WHP SAC Tech. Rep. No. 3, WOCE Rep. 162/98, 48 pp.

Haine, T., and J. Marshall, 1998: Gravitational, symmetric and baroclinic instability of the ocean mixed layer. *J. Phys. Oceanogr.,* **28,** 634–658.

Haynes, P. H., 1985: Nonlinear instability of a Rossby-wave critical layer. *J. Fluid Mech.,* **161,** 493–511.

——, and E. Shuckburgh, 2000a: Effective diffusivity as a diagnostic of atmospheric transport 1: Stratosphere. *J. Geophys. Res.,* **105** (D18), 22 777–22 794.

——, and ——, 2000b: Effective diffusivity as a diagnostic of atmospheric transport 2: Troposphere and lower stratosphere. *J. Geophys. Res.,* **105** (D18), 22 795–22 810.

Holloway, G., 1986: Estimation of oceanic eddy transports from satellite altimetry. *Nature,* **323,** 243–244.

Juckes, M., and M. McIntyre, 1987: A high resolution one-layer model of breaking planetary waves in the stratosphere. *Nature,* **328,** 590–596.

Karsten, R., and J. Marshall, 2002: Constructing the residual circulation of the Antarctic Circumpolar Current from observations. *J. Phys. Oceanogr.,* **32,** 3315–3327.

Keffer, T., and G. Holloway, 1988: Estimating Southern Ocean eddy flux of heat and salt from satellite altimetry. *Nature,* **332,** 624–626.

Kushner, P. J., and I. M. Held, 1998: A test, using atmospheric data of a method for estimating oceanic eddy diffusivity. *Geophys. Res. Lett.,* **25,** 4213–4216.

Lemoine, F., and Coauthors, 1997: The development of the NASA GSFC and NIMA Joint Geophysical Model. *Gravity, Geoid and Marine Geodesy,* J. Segawa et al., Eds., Vol. 117, *International Association of Geodesy Symposia,* Springer Verlag, 461–469.

Le Traon, P.-Y., and F. Ogor, 1998: ERS-1/2 orbit error improvement using TOPEX/Poseidon: The 2 cm challenge. *J. Geophys. Res.,* **103,** 8045–8057.

——, F. Nadal, and N. Ducet, 1998: An improved mapping method of multisatellite altimeter data. *J. Atmos. Oceanic Technol.,* **15,** 522–534.

Lumpkin, R., A.-M. Treguier, and K. Speer, 2002: Lagrangian eddy scales in the Northern Atlantic Ocean. *J. Phys. Oceanogr.,* **32,** 2425–2440.

Majda, A. J., and P. R. Kramer, 1999: Simplified models for turbulent diffusion: Theory, numerical modeling and physical phenomena. *Phys. Rep.,* **314,** 237–274.

Marshall, D., 1997: Subduction of water masses in an eddying ocean. *J. Mar. Res.,* **55,** 201–222.

Marshall, J. C., and G. J. Shutts, 1981: A note on rotational and divergent eddy fluxes. *J. Phys. Oceanogr.,* **11,** 1677–1680.

——, and T. Radko, 2003: Residual mean solutions for the Antarctic Circumpolar Current and its associated overturning circulation. *J. Phys. Oceanogr.,* **33,** 2341–2354.

——, D. Olbers, D. Wolf-Gladrow, and H. Ross, 1993: Potential vorticity constraints on the dynamics and hydrography of the Southern Ocean. *J. Phys. Oceanogr.,* **23,** 465–487.

——, A. Adcroft, C. Hill, L. Perelman, and C. Heisey, 1997: A finite-volume, incompressible Navier Stokes model for studies of the ocean on parallel computers. *J. Geophys. Res.,* **102** (C3), 5753–5766.

——, D. Jamous, and J. Nilsson, 1999: Reconciling 'thermodynamic' and 'dynamic' methods of computation of water-mass transformation rates. *Deep-Sea Res. I,* **46,** 545–572.

Nakamura, N., 1996: Two-dimensional mixing, edge-formation, and permeability diagnosed in area coordinates. *J. Atmos. Sci.,* **53,** 1524–1537.

——, and J. Ma, 1997: Modified Lagrangian-mean diagnostics of the stratospheric polar vortices: 2. Nitrous oxide and seasonal barrier migration in the cryogenic limb array etalon spectrometer and SKYHI general circulation model. *J. Geophys. Res.,* **102,** 25 721–25 736.

Olbers, D., and M. Visbeck, 2005: A model of the zonally averaged stratification and overturning of the southern ocean. *J. Phys. Oceanogr.,* **35,** 1190–1205.

——, D. Borowski, C. Volker, and J. O. Wolff, 2004: The dynamical balance, transport and circulation of the Antarctic Circumpolar Current. *Antarctic Sci.,* **16,** 439–470.

Pierrehumbert, R. T., 2000: Lattice models of advection-diffusion. *Chaos,* **10,** 61–74.

Plumb, R., and R. Ferrari, 2005: Transformed Eulerian-mean theory. Part I: Nonquasigeostrophic theory for eddies on a zonal-mean flow. *J. Phys. Oceanogr.,* **35,** 165–174.

Rhines, P., and W. R. Young, 1983: How rapidly is a passive scalar mixed within closed streamlines? *J. Fluid Mech.,* **133,** 133–145.

Rintoul, S., C. Hughes, and D. Olbers, 2001: The Antarctic Circumpolar Current System. *Ocean Circulation and Climate: Observing and Modeling the Global Ocean,* G. Siedler, J. Church, and J. Gould, Eds., International Geophysics Series, Vol. 77, Academic Press, 271–302.

Shuckburgh, E. F., and P. H. Haynes, 2003: Diagnosing transport and mixing using a tracer-based coordinate system. *Phys. Fluids,* **15,** 3342–3357.

Speer, K., S. R. Rintoul, and B. Sloyan, 2000: The diabatic Deacon cell. *J. Phys. Oceanogr.,* **30,** 3212–3222.

Stammer, D., 1998: On eddy characteristics, eddy transports, and mean flow properties. *J. Phys. Oceanogr.,* **28,** 727–739.

Treguier, A. M., I. M. Held, and V. D. Larichev, 1997: Parameterization of quasigeostrophic eddies in primitive equation ocean models. *J. Phys. Oceanogr.,* **27,** 567–580.

Walin, G., 1982: On the relation between sea-surface heat flow and thermal circulation in the ocean. *Tellus,* **34,** 187–195.

Winters, K. B., and E. A. D'Asaro, 1996: Diascular flux and the rate of fluid mixing. *J. Fluid Mech.,* **317,** 179–193.

Zurbas, V., and I. S. Oh, 2004: Drifter-derived maps of lateral diffusivity in the Pacific and Atlantic Oceans in relation to surface circulation patterns. *J. Geophys. Res.,* **109,** C05015, doi:10.1029/2003JC002241.